Multi-Scale Multiphysics Simulation of Metal L-PBF AM Process and Subsequent Mechanical Analysis

Bayat, M.; De Baere, D.; Mohanty, S.; Hattel, J. H.

Publication date:
2018

Document Version
Peer reviewed version

MULTI-SCALE MULTIPHYSICS SIMULATION OF METAL L-PBF AM PROCESS AND SUBSEQUENT MECHANICAL ANALYSIS

M. BAYAT*, D. DE BAERE*, S. MOHANTY* AND J. H. HATTEL*

** Department of Mechanical Engineering, Technical University of Denmark, building 425, room 225, Lyngby, Denmark*

ABSTRACT

In this paper, a multi-physics numerical model for multi-track-multi-layer laser powder bed fusion (L-PBF) process is developed and used for analysing the formation and evolution of porosities caused by lack of fusion and improper melting. The simulations are divided into two categories: first and foremost, a multi-physics thermo-fluid model in meso-scale, and second, a mechanical model based on the concept of a unit cell. The thermo-fluid model is used to track and observe the formation of the porosities, and considers phenomena such as multi-phase flow, melting/solidification, radiation heat transfer, capillary and thermo-capillary (Marangoni effect) forces, recoil pressure, geometry dependant absorptivity, and finally evaporation and evaporative cooling. The results for the investigated process parameters indicate that the porosities are mainly formed due to improper fusion of the particles. The probability of presence of pores is also observed to be higher in the first layers. Moreover, the lack of fusion zones are seen to become smaller in the subsequent layers, largely due to better fluid flow and higher temperatures in those layers. Based on the porosity levels determined from the thermo-fluid model, a unit cell mechanical model with an equivalent amount of porosity has been made and subsequently subjected to loading for analysing the part's mechanical behaviour. The unit cell results show that an increase in the porosity can highly affect and deteriorate the part's elastic modulus and its yield strength, as well. The combination of the thermo-fluid and the mechanical unit cell model establishes a direct link between process parameters and mechanical properties for L-PBF.

Keywords: process-property correlation, multi-physics model, thermo-fluid model, multi-layer L-PBF, porosity formation, unit cell approach.

INTRODUCION

Laser powder bed fusion (L-PBF) method, is categorized as a metal additive manufacturing process [1], where the metallic parts are produced in a layer-wise manner. A simple view of a typical L-PBF machine is shown in Fig. 1. In this process, first a layer of fine spherical metallic particles, whose diameters typically span from approximately 10 μm to 60 μm [2], is distributed on a base plate (which in turn is attached to a build platform) by means of a controllable coating mechanism. Then, the laser starts scanning predefined locations based on the data provided in the CAD files [3]. While the laser scans these zones, the fine metallic particles will get coalesced together, either by being sintered or fully-molten, depending on

the intensity of the laser power. After the first layer is shaped, the build platform moves down and another layer of powder is laid down. Subsequently, the powder feeding and laser scanning continues until the whole part is manufactured [4].

L-PBF has many advantages over the conventional production methods (e.g. Casting, milling, etc) and outweighs them in certain areas such as design freedom, material waste, manufacturing time, etc [5]. However, some of the parts that are manufactured by this process, still suffer from major defects, such as, denudation zones [6], keyhole porosities [7], surface porosities [8] and voids [9].

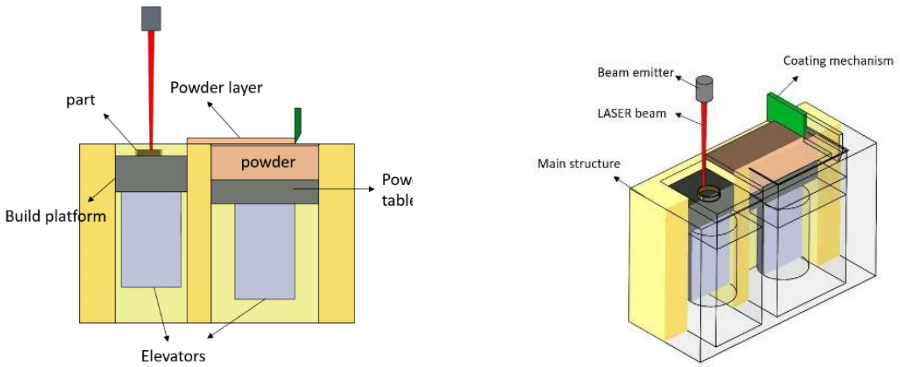

Fig. 1 L-PBF machine along with its components; (left) cross section and (right) 3-D views.

Depending on the range of the processing parameters (e.g. scanning speed, laser power, hatch distance, etc), the shape and dimensions of the defects might differ considerably. For example, low linear energy density (LED) can result in surface defects as well as lack of fusion zones with unsintered particles [8]. Adoption of high LED levels causes overheated sites that ultimately lead to internal metallurgical or keyhole voids [10].

In the recent years, advanced online monitoring systems have been developed for analysing the thermal maps [11], the solidification time as well as the keyhole evolution [12] during the L-PBF process. However, these research methods, depending on their illumination source and degree of complexity, can either be highly expensive or constitute high safety risks [13].

In the current scenario, developing a multi-physics numerical model for L-PBF process that can predict the evolution of the internal pores can improve the predictability of the process to a large extent. From a numerical point of view, L-PBF contains many physical phenomena, such as: evaporation, melting/solidification, thermal radiation, laser absorption, liquid metal flow, recoil pressure, etc. Numerical models have been developed to address these phenomena, and depending on the complexity and governing physics, they can be categorised into thermal models [14]–[16], thermo-fluid models [17]–[19], thermo-microstructural models [20], [21] and thermo-mechanical models [22]. In particular, thermo-fluid models are best suited for observing the formation and evolution of porosity during the laser powder bed fusion process. Such information regarding the distribution of voids/pores can further be utilized to predict the mechanical response of the corresponding parts through the representative volume element and unit cell methods. Accordingly, by means of these

approaches, one might be able to investigate the effect of different patterns of voids or added elements on the overall mechanical response of the parts [23], [24].

In this paper, a multi-physics numerical model for the L-PBF process has been developed which covers multi-phase flow, solidification/melting, evaporation, recoil pressure, capillary forces, Marangoni effect, buoyancy effect, ray tracing method, radiation and flow in porous medium. The formation of lack-of-fusion defects during the multi-track and multi-layer L-PBF process has been investigated using said model. Moreover, to simulate the actual stochastic distribution of powder layers, a discrete element method (DEM) has been implemented that tracks the position of the powder particles during the powder-feeding step. To consider the effects of surface elevation of the previous sintered/fused layers on the current powder layer's distribution, the results of thermo-fluid simulation of each layer have been exported as CAD data for usage in the DEM simulations. Eventually, the calculated porosity level for all layers has been used to make an equivalent unit cell to study the effect of the porosity on the mechanical behaviour of the samples. An image analysis has been performed on the fluid fraction data to calculate the porosity levels needed for unit cell model.

NUMERICAL MODEL

During the L-PBF process, usually a relatively high amount of power (50-1000 W) [2] is concentrated on a small surface area, which can easily melt down and even evaporate the powder layer. Physical phenomena such as recoil pressure, capillary and thermo-capillary forces prevail in those harsh conditions and highly affect the material's flow behaviour. To determine the temperature field and observe the material's flow inside the melt regions, it becomes necessary to solve the coupled partial differential equations of balance of mass, linear momentum and energy together. This has been implemented in the thermo-fluid model developed using the commercial software Flow-3D, which in-turn is based on the finite volume method (FVM). Moreover, to better simulate the thermal interaction between laser rays and the fluid (powder and base metal), a ray-tracing method along with a geometry-dependant absorptivity has been implemented. In the following section of the paper, the governing equations for the thermo-fluid model are first described and a detailed description about the laser-material model is also given. Subsequently, the mechanical model for analysing the material behaviour with the unit cell approach and its governing equations are described. The mechanical model has been implemented on the commercial software ABAQUS version 6.16 which works based on the finite element method.

GOVERNING PHYSICS: THERMO-FLUID MODEL

Fluid flow motion

The computational domain is divided into two immiscible phases i.e. the ambient air and the metal regions (labelled as void and fluid respectively). Several methods are available in

literature to track the free surface of each phase, such as level-set [25], phase field and volume of fluid (VOF) [26] in a fixed mesh (Eulerian framework) approach and Stephan's problem in a moving mesh (Lagrangian framework) approach. In this work, the VOF method has been used for tracking the phase interface. According to the VOF method, the mass balance equation for two-phase flow can be expressed as [26]:

$$\frac{\partial}{\partial t}(\alpha_F \rho_F) + \vec{\nabla}.\left(\alpha_F \rho_F \vec{V}\right) = -\dot{m}_{lv} \tag{1}$$

where the subscript $(\,)_F$ stands for the fluid phase, ρ ($\frac{\mathrm{kg}}{\mathrm{m}^3}$) is the density and $\dot{m}_{lv}$ ($\frac{\mathrm{kg}}{\mathrm{m}^3.\mathrm{s}}$) is the volumetric rate of mass loss by evaporation. α_F shows the volume fraction of the fluid phase. To solve equation (1), it is necessary to fulfil the condition that the summation of volume fractions of all present phases equals unity:

$$\alpha_F + \alpha_V = 1 \tag{2}$$

where the subscript $(\,)_V$ demonstrates the void phase. This condition also holds an important physical meaning that the cells must not become empty of a medium.

To determine the pressure-velocity field, the system of equations of balance of linear momentum should be solved along with (1) and (2):

$$\rho\left[\frac{\partial}{\partial t}\left(\vec{V}\right) + \vec{V}.\vec{\nabla}\vec{V}\right] = -\vec{\nabla}P + \vec{F}_s + \vec{F}_V + \vec{F}_\theta \tag{3}$$

where V is the velocity vector and the two vectors $\overrightarrow{F_S}$ and $\overrightarrow{F_V}$ stand for the volumetric forces caused by the spatial variation in fluid stress tensor and solidification drag forces based on Darcy's law for porous medium [27]. The vector of the volumetric forces caused by the spatial variation in internal stresses is defined as:

$$\overrightarrow{F_S} = \vec{\nabla}.[\tau_{ij}] \tag{4}$$

where $[\tau_{ij}]$ is the internal stress tensor and is defined as:

$$\tau_{ij} = 2\mu\left[\frac{1}{2}\left(V_{i,j} + V_{j,i}\right) - \frac{1}{3}\delta_{ij}V_{,k}\right] \tag{5}$$

where δ_{ij} is the delta Dirac function. The last term in equation (5) will diminish due to the incompressibility of the present fluid. Since the flow is two-phase, the average values for viscosity and density are used, defined by means of a simple mixing rule:

$$\mu = \alpha_F \mu_F + \alpha_V \mu_V \tag{6}$$

$$\rho = \alpha_F \rho_F + \alpha_V \rho_V \tag{7}$$

To model the moving solidification front, the volumetric forces are defined to be highly dependent on the liquid fraction of the fluid. These forces, also called the solidification drag forces, are supposed to free and freeze the fluid flow depending upon the fluid liquid fraction [28]:

$$\vec{F}_V = -c\frac{(1-f_l)^2}{B + f_l^3}.\vec{V} \tag{8}$$

where c $\left[\frac{\mathrm{kg}}{\mathrm{m}^3.\mathrm{s}}\right]$ and B $[-]$ are the Karman-Cozeny constants, which, depending on the application, are in the range of $10^5 - 10^7$and $10^{-5} - 10^{-3}$ respectively. Interestingly, the

solidification drag forces, according to equation (8), are in the opposite direction of the velocity vectors. Thus, a decrease in liquid volume fraction dramatically increases these forces to an extent that is sufficiently high to freeze the fluid motion.

The last term in equation (3) is the volumetric force which is being imposed on the fluid due to the buoyancy effect. In this work, since the flow is assumed to be incompressible, the Boussinesq approximation is used for calculating the buoyancy force:

$$F_\theta = \rho g \beta (T - T_l) \tag{9}$$

where β $(\frac{1}{\mathrm{K}})$ and T_l are the expansion coefficient and the fluid's liquidus temperature, respectively, and g $(\frac{\mathrm{m}}{\mathrm{s}^2})$ is the gravitational acceleration.

Heat transfer and solidification

The energy balance equation is applied to the computational domain and subsequently coupled to the velocity field, to find the temperature field and the fluid's fusion condition (liquid or solid state):

$$\rho \left[\frac{\partial (H)}{\partial t} + \vec{V}.\vec{\nabla} H\right] = \vec{\nabla}.\left(k\vec{\nabla} T\right) - \dot{q}'''_{evap}. \tag{10}$$

where $\dot{q}'''_{evap}$ $(\frac{\mathrm{W}}{\mathrm{m}^3})$ is the volumetric heat sink due to the evaporative cooling of fluid and H $(\frac{\mathrm{kJ}}{\mathrm{kg}})$ is called the sensible enthalpy that can be expressed as:

$$H = h_{ref} + \int_{T=T_{amb}}^{T} C_p dT + f_l \Delta H_{sl}, \tag{11}$$

where h_{ref} $(\frac{\mathrm{kJ}}{\mathrm{kg}})$ and ΔH_{sl} $(\frac{\mathrm{kJ}}{\mathrm{kg}})$ stand for the reference specific enthalpy of the fluid and the latent heat of fusion, respectively. The enthalpy-porosity method, which has been widely used for melting/solidification modelling [29], is also used in this study. It is assumed that, for the current metal, liquid volume fraction is a linear function of temperature during the solidification interval:

$$f_l = \begin{cases} 0 & , T < T_s \\ \dfrac{T - T_s}{T_l - T_s} & , T_s < T < T_l \\ 1 & , T_l < T. \end{cases} \tag{12}$$

Since the problem is assumed to be a multi-phase flow, the average sensible enthalpy is used in the heat balance equation, which can be determined by a mixing rule as:

$$H = \frac{\rho_F \alpha_F H_F + \rho_V \alpha_V H_V}{\rho_F \alpha_F + \rho_V \alpha_V} \tag{13}$$

Recoil, capillary and thermo-capillary forces

During the L-PBF and welding processes, since high-density heat fluxes are imposed on the fluid's surface, elevated temperatures are attained which cause the material to boil and evaporate. The vaporization of the metal will impart a negative force against the fluid surface, largely due to momentum balance with the escaping vaporized metal, called as the recoil pressure which in extreme cases can even lead to formation of deep keyholes. On the other hand, localized elevated temperature fields will cause large thermal gradients which will subsequently result in thermally-induced shear stresses on the exposed surfaces of the fluid (Marangoni effect). Furthermore, due to the large deflections of the fluid surfaces, capillary forces are also dominant and can affect the fluid motion, especially on the places where big curvatures are formed.

In principal, the saturation pressure of a fluid can be determined by means of thermodynamic relations and equations of state. However, empirical correlations can also be used to find the saturation pressure with a good accuracy, such as the Clausius-Clapeyron equation:

$$P_{sat}(T) = P_{atm}\exp\left[\frac{\Delta H_{lv}}{C_v(\gamma-1)}\left(\frac{1}{T_g}-\frac{1}{T}\right)\right], \tag{14}$$

where P_{atm} and T_g in equation (14) are the atmospheric pressure and the fluid's saturation temperature (boiling temperature) at this pressure, respectively. ΔH_{lv} $(\frac{\text{kJ}}{\text{kg}})$ is the latent heat of vaporization and C_v $(\frac{\text{kJ}}{\text{kg.K}})$ is the specific heat capacity of vaporized fluid at constant volume. There have been a number of investigations on the recoil pressure, and in this study the recoil pressure is assumed to be a function of saturation pressure [30]:

$$P_{recoil}(T) = 0.54P_{sat}(T), \tag{15}$$

The recoil pressure will thus increase exponentially with increase in temperature beyond the boiling point. According to the statistical thermodynamics, the evaporative mass rate can be approximated as [18]:

$$\dot{m}_{lv} = A_{acom}.\sqrt{\frac{M}{2\pi\bar{R}T}}.P_{sat}(T), \tag{16}$$

where A_{accom} and $\bar{R}$ $(\frac{\text{kJ}}{\text{kmole.K}})$ are the accommodation coefficient and the universal gas constant respectively. The thermally-induced shear stresses can be expressed as:

$$\tau = -\vec{\nabla}_s T.\frac{d\sigma}{dT}. \tag{17}$$

In equation (17), $\vec{\nabla}_s T$ $(\frac{\text{K}}{\text{m}})$ shows the planar (tangent to the interface) temperature gradient of the fluid and $\frac{d\sigma}{dT}$ $(\frac{\text{N}}{\text{m.K}})$ represents the temperature dependency of the surface tension. Furthermore, as mentioned before, since the fluid surface might not be smooth, the capillary forces are also present:

$$P_{cap} = \sigma.\kappa. \tag{18}$$

In equation (18), σ $\left(\frac{\mathrm{N}}{\mathrm{m}}\right)$ and κ $\left(\frac{1}{\mathrm{m}}\right)$ are the surface tension between the two phases and the curvature of the free surface respectively. From a mathematical point of view, the mentioned triple forces can be expressed in a single vector form as:

$$F_{V/F}\ (Pa) = [P_{recoil} + \sigma.\kappa]\vec{n} - \left[\vec{\nabla}T - \vec{n}(\vec{\nabla}T.\vec{n})\right]\frac{d\sigma}{dT} \tag{19}$$

According to equation (19), the recoil and capillary effects act as an jump in the pressure on the void/fluid interface and are always normal to the free surface [31]. On the other hand, the thermally-induced shear stresses, as can be seen on the right side of equation (19), are tangent to the free surface. Also, depending on the sign of temperature dependency of the surface tension, the flow might be driven radially outward or inward. $\vec{n}$ is the void/fluid interface normal vector and is calculated as:

$$\vec{n} = \frac{\vec{\nabla}\varphi}{|\vec{\nabla}\varphi|} \tag{20}$$

where φ is a scalar function which shows the elevation of the void/fluid interface. The curvature mentioned in equation (20) can be determined by:

$$\kappa = -\left[\nabla.\left(\frac{\vec{n}}{|\vec{n}|}\right)\right] = \frac{1}{|\vec{n}|}\left[\left(\frac{\vec{n}.\vec{\nabla}}{|\vec{n}|}\right)|\vec{n}| - (\vec{\nabla}.\vec{n})\right] \tag{21}$$

The mentioned forces are all imposed on the Ω boundary, shown in Fig. 2, along with the imposed thermal boundary conditions.

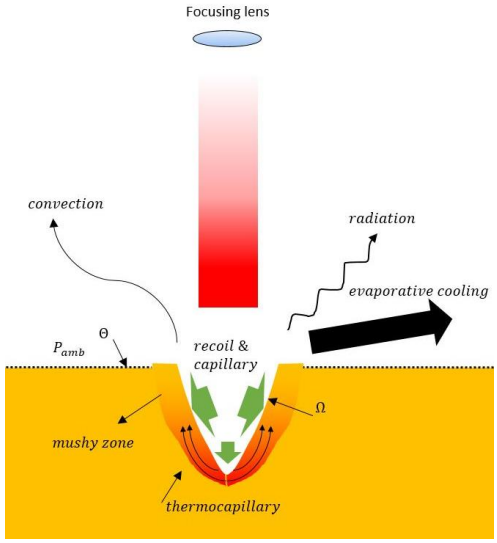

Fig. 2 Schematic view of the recoil pressure, capillary and thermo-capillary forces along with the thermal boundary conditions on the Ω boundary.

Fig. 2 also shows an overall view of the present boundary conditions, where the top boundary is assumed to be a pressure outlet boundary condition, and set to ambient atmospheric pressure allowing both phases to escape the control volume if necessary.

Furthermore, the laser also irradiates the interface, so the thermal boundary condition on this layer can be expressed as:

$$-k\frac{\partial T}{\partial \vec{n}} + \varepsilon\sigma(T_{amb}^4 - T^4) + h_{amb}(T_{amb} - T) + Q''_{i,j} = 0 \tag{22}$$

where ε and σ ($\frac{\mathrm{W}}{\mathrm{m^2.K^4}}$) are the fluid's surface emissivity and the Stephan-Boltzmann constants respectively. $h_{amb}(\frac{\mathrm{W}}{\mathrm{m^2.K}})$ stands for the convective heat transfer coefficient of the void. Q''_{ij} in equation (22) is the heat flux of the laser ray "i" after "j" number of recorded collisions.

Laser-material interaction

Depending on the application, there are several ways to model the effect of the laser on the thermal behaviour of the material, such as moving point source, moving heat flux, moving volumetric heat source, equivalent moving volumetric heat source based on optical penetration depth (OPD) and finally ray tracing method. In this work, to better simulate the actual laser-material interaction, the ray-tracing method, along with a geometry-dependent absorptivity, are used. The laser heat flux, which is being emitted from the focusing lens shown in Fig. 2, is assumed to have a planar Gaussian distribution with the following mathematical function:

$$q''_{laser}(x,y) = \frac{2P}{\pi R^2}\exp\left(-\frac{2((x-x_{las})^2 + (y-y_{las})^2)}{R^2}\right), \tag{23}$$

where R is the beam radius and x_{las}, y_{las} show the position of the moving laser beam. Depending on the resolution of the computational domain, the analytical expression of the heat flux in equation (23) will be divided into a number of smaller parts while retaining the total beam energy. For each incident ray "i", the new direction of the reflected rays $\vec{e}_{i,j+1}$ for the "j" th collision is determined based on the ray-tracing method as follows:

$$\vec{e}_{i,j+1} = \vec{e}_{i,j} - 2(\vec{e}_{i,j}.\vec{n}_{i,j})\vec{n}_{i,j} \tag{24}$$

The absorptivity of the laser ray at each collision is then assumed to be a geometry-dependant cosine function of the incident angle in this work..

GOVERNING PHYSICS: MECHANICAL MODEL

The equilibrium equation is the principal governing partial differential equation which defines the relationship between the applied forces and the material's mechanical response,

$$\nabla.\sigma_{ij} = 0, \tag{25}$$

where σ_{ij} is the stress tensor in equation (25). The total strain tensor ε_{ij}^{tot} can be decomposed into elastic and plastic parts:

$$\varepsilon_{ij}^{tot} = \varepsilon_{ij}^{el} + \varepsilon_{ij}^{pl}, \tag{26}$$

where $()_{el}$, $()_{pl}$ are subscripts standing for elastic and plastic behaviour respectively. The elastic strain is calculated based on the general Hooke's law:

$$\sigma_{ij} = \frac{E}{1+v}\left[\frac{1}{2}\left(\delta_{ik}\delta_{jl} + \delta_{il}\delta_{jk}\right) + \frac{v}{1-2v}\delta_{ij}\delta_{kl}\right]\varepsilon_{kl}^{el}. \quad (27)$$

where E (Pa) and v are elastic modulus and Poisson's ratio, respectively. The J2 flow theory defines the mechanical behaviour of the material in the plastic zone. The corresponding plastic strain increment is calculated as:

$$\dot{\varepsilon}_{ij}^{pl} = \frac{9}{4}\left[\frac{1}{E_t} - \frac{1}{E}\right]\frac{s_{kl}\dot{\sigma}_{kl}}{\sigma_e^2}s_{ij}. \quad (28)$$

where E_t (Pa) is the tangent modulus of the material, s_{ij} is the deviatoric stress tensor and σ_e is the equivalent Mises stress.

$$s_{ij} = \sigma_{ij} - \frac{1}{3}tr\left(\sigma_{ij}\right), \quad (29)$$

$$\sigma_e = \sqrt{\frac{3}{2}s_{ij}s_{ij}}. \quad (30)$$

METHODOLOGY

As already discussed in the introduction, the L-PBF process consists of two primary steps, namely powder-laying and fusion. In this work, to determine the position of the solid particles during the powder-laying step, a discrete element method (DEM) is used, as shown in Fig. 3. After the DEM simulation, the CAD file containing the laid powder layer is extracted by an in-house code and imported as a fluid region into the thermo-fluid model (fusion model). After the thermo-fluid calculations, the CAD file of the fluid region, along with its stored thermal data, are extracted and the former is fed to the next powder-laying calculation model where it serves as a solid wall with a prescribed restitution coefficient. The latter is used as the initial thermal and fluid boundary condition for the next thermo-fluid (fusion) model. This procedure is repeated for three layers.

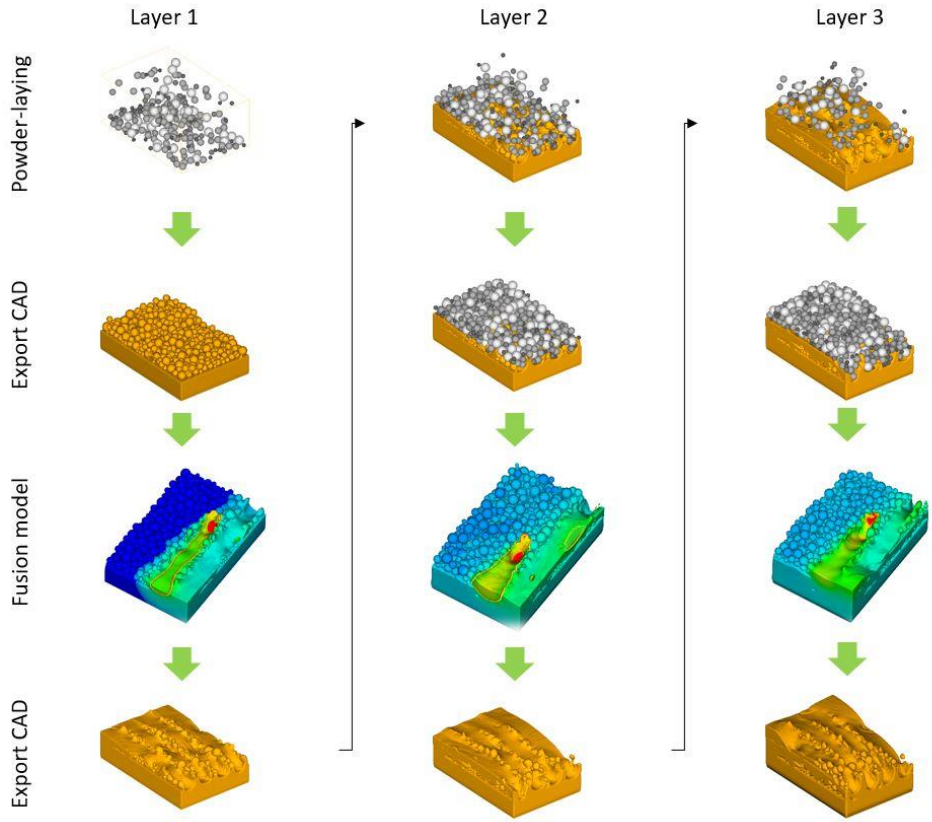

Fig. 3 The methodology used for the powder-laying and fusion calculations.

To assess the influence of the lack-of-fusion induced porosities on the mechanical behaviour of the manufactured samples, a unit cell approach is implemented in this work. This unit cell method is used to study the effect of porosities on both the yield stress and the elastic modulus of the samples. First, several cross-sections are made from the 3D CAD geometry extracted from the thermo-fluid model, and the section contours (showing the value of fluid fraction) are transformed into monochromic images. Subsequently, the images are processed by a numerical code developed to determine the amount of porosity in these cross-sections.

Next, a simplified unit cell geometry, i.e. a square with 500 μm edge length, is constructed with a hole (equivalent to the determined porosity) in the middle of the sample. This unit cell is then subjected to the mechanical boundary conditions and loads shown in Fig. 4. The left and bottom boundaries are x-symmetry and y-symmetry respectively, while a uniform x-displacement is imposed on the right boundary in an incremental manner. While the cell is being loaded, the average force on the right boundary is determined. At the same time, the average strain is also calculated, which is defined as the ratio of the x-displacement to the characteristic length of the unit cell.

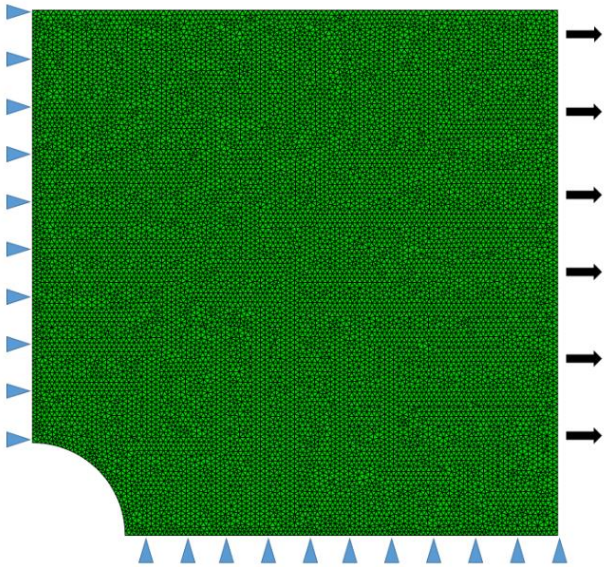

Fig. 4. Mechanical boundary conditions for the unit cell.

RESULTS AND DISCUSSIONS

THERMAL FIELDS AND FLUID FLOW

The process parameters and the laser specifications used in this study are all gathered in Table 1. The temperature field during the scanning of first layer along with the melt region are both shown in Fig. 5 for different times.

Table 1. Process parameters for the multi-layer simulation

Parameter	Value	Parameter	Value
Hatch spacing	100 µm	Scanning speed	1600 mm/s
Beam size	60 µm	Layer thickness	40 µm
Beam power	150 W	Scan length	1000 µm

According to Fig. 5 (a), the maximum temperature zone is formed very close to the centre of the moving laser beam. At 400 µs, most of the powder and base-plate are still at their initial temperature of 300 K. Due to the relatively high scanning velocity of the laser and the presence of air between the powders, the flow (propagation) of the heat in the transverse direction is much slower. On the other hand, the thermal resistance of the material (at $t > 300$ µs) on the right side of the scanning beam, is much lower than that of the unmelted powders due to the dense morphology of the metal.

The melt region contour during the scanning of the first layer is also shown in Fig. 5 (b). At t = 860 μs, it can be clearly observed that the melt region of the two neighbouring tracks do not reach each other and accordingly, lack of fusion sites and unsintered particles are formed between the tracks.

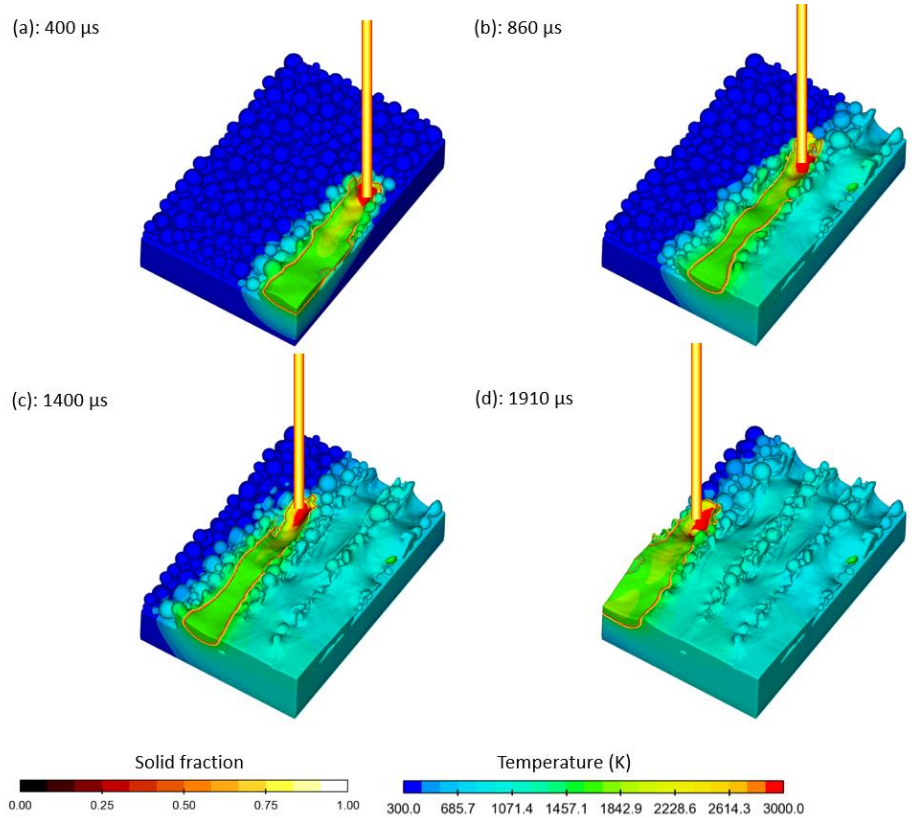

Fig. 5 Thermal field and melt region during the scanning of the first layer of the powder.

Corresponding to Fig. 5 (c) at t = 1400 μs, a hole is formed close to the position of the centre of the laser beam. When the temperature in the region goes above the saturation temperature of the metal, the recoil pressure becomes dominant, pushes the deformable liquid down and makes a keyhole. The size of the keyhole increases with further increase in temperature due to greater recoil pressure.

The melting of powder particles during L-PBF is caused either via direct contact with the laser rays or via contact with a hot return flow formed due to the negative pressure gradient present on the fusion front. Starting with the former pathway, when the laser irradiates the powder for the first time, the powder begins to melt, as observed in Fig. 6 (a) and (b), and gains a high flowability. Due to the presence of recoil pressure, the Marangoni effect and the incompressibility of the flow, a large pressure is formed on this front (i.e. the melting front), as shown in the pressure contours in Fig. 7 in the x-z plane.

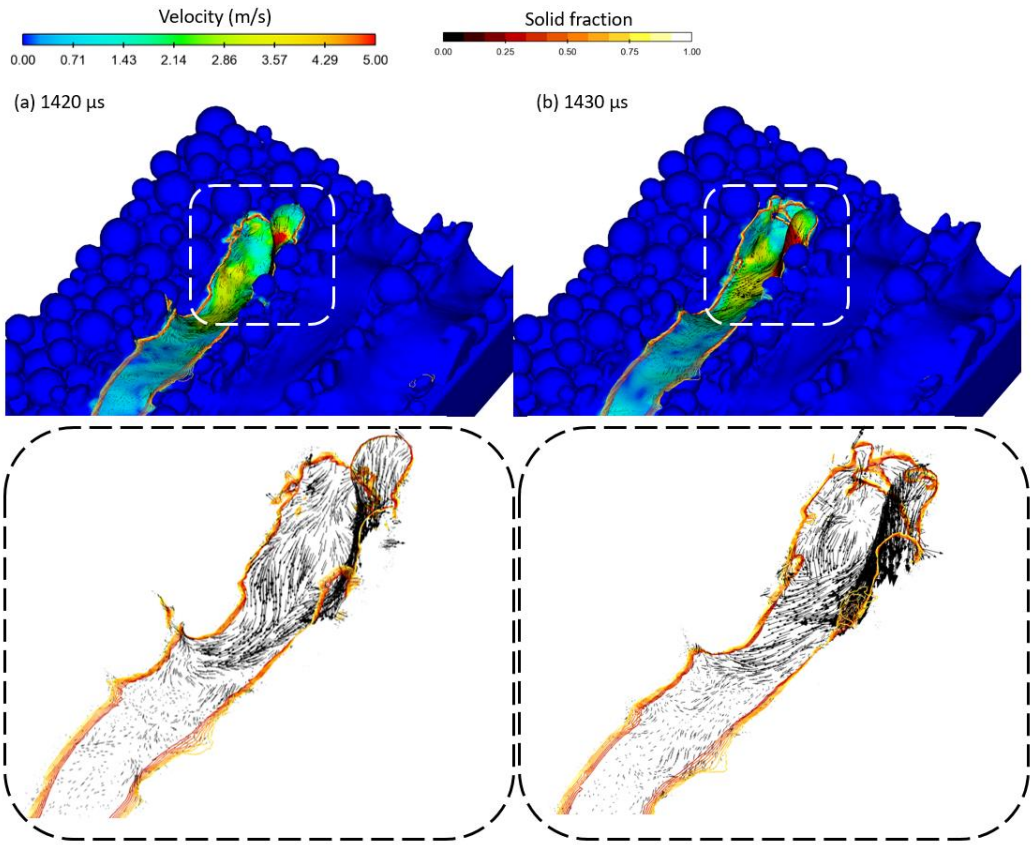

Fig. 6. Fluid velocity magnitude and melt region for the first layer at (a) 1420 μs and (b) 1430 μs.

This high-pressure front formed ahead of the laser beam drives the hot fluid (metal) backwards to the already molten zones (see Fig. 6 (a)), thus widening the melt track. As shown in Fig. 7, the coexistence of a high pressure zone in front of the melt pool and a low-pressure one at its rear, forms a local pressure gradient which serves as a driver of hot metal flow back to the relatively colder melted regions.

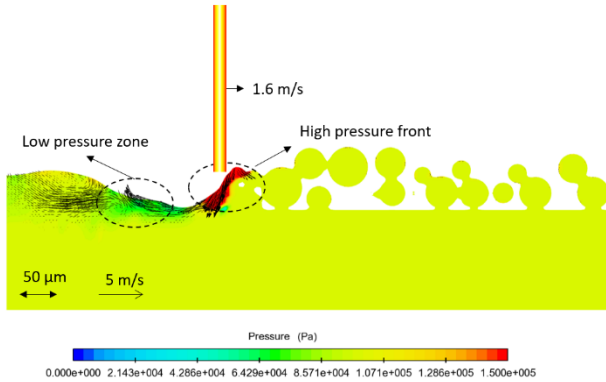

Fig. 7. Pressure front formed ahead of the laser beam for x-z plane.

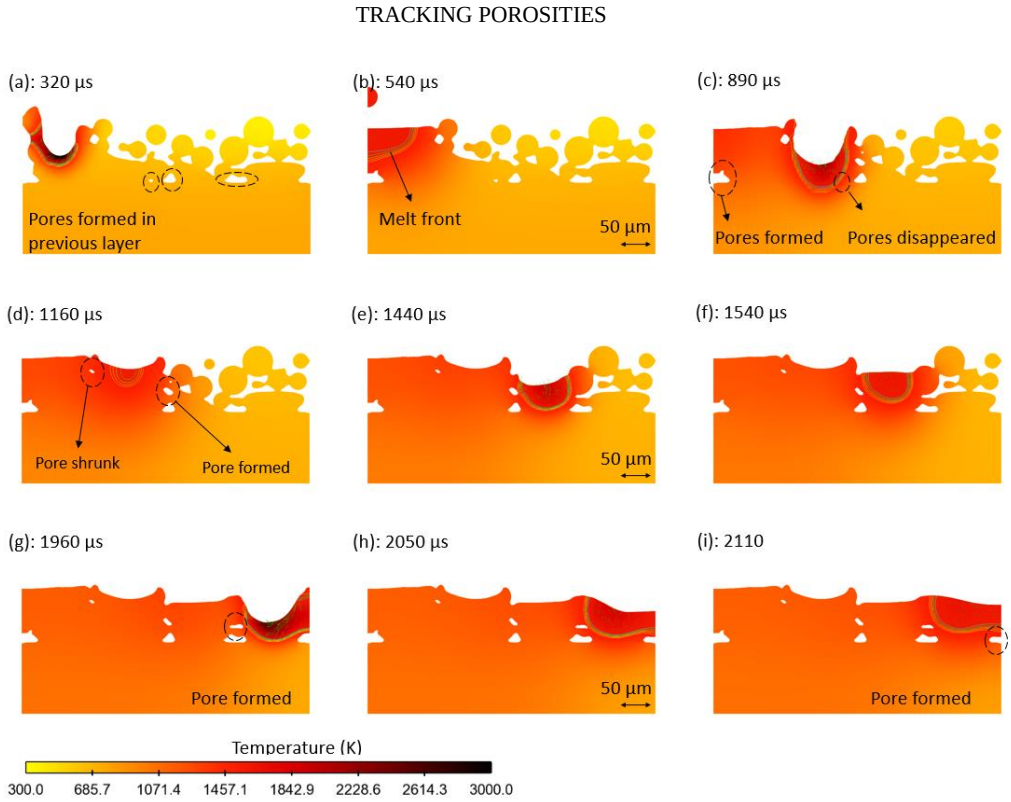

Fig. 8. Fluid region, temperature contour and melt pool dynamics during the scanning of the second layer at x=200 µm (transverse cross-section) for (a): 320 µs, (b) 540 µs, (c) 890 µs, (d) 1160 µs, (e) 1440 µs, (f) 1540 µs, (g) 1960 µs, (h) 2050 µs, (i) 2110 µs.

To track how the lack-of-fusion porosities are formed and how they evolve, multiple cross-sections are made in different planes from the 3D domain. Fig. 8. Fluid region, temperature contour and melt pool dynamics during the scanning of the second layer at x=200 μm (transverse cross-section) shows the fluid region along with its thermal field during the scanning of the second layer at different times on one of the transverse cross-sections (with respect to direction of laser movement). At t = 320 μs, the centre of the laser beam reaches the position of the cross-section, and correspondingly the highest temperatures are observed.

At t = 540 μs, when the laser is farther away from this plane, the melt pool starts to cool down and solidify at the same time. At t = 890 μs, the laser again reaches the plane while scanning the second track. The keyhole formed due to presence of recoil pressure becomes sufficiently deep to capture some of the pores from the previous layer.

At t = 1160 μs, subsequent to the collapse of the keyhole walls and solidification of the melt region, another pore is observed to have been formed at the top right side of the track. Simultaneously, some of the pores initially formed at t = 890 μs are now observed to have shrunk in size. At t = 1960 μs and 2110 μs, a number of pores are also formed due to the air being trapped below the melt pool. Although these pores have a strong potential to escape the fluid region (because of large density-driven buoyancy force), they cannot move upwards as they are entrapped in either the mushy or the solid zone.

On the other hand, there are a number of occasions where the pores formed during the scanning of the previous layers, coalesce or escape the fluid surface, as shown in Fig. 9.

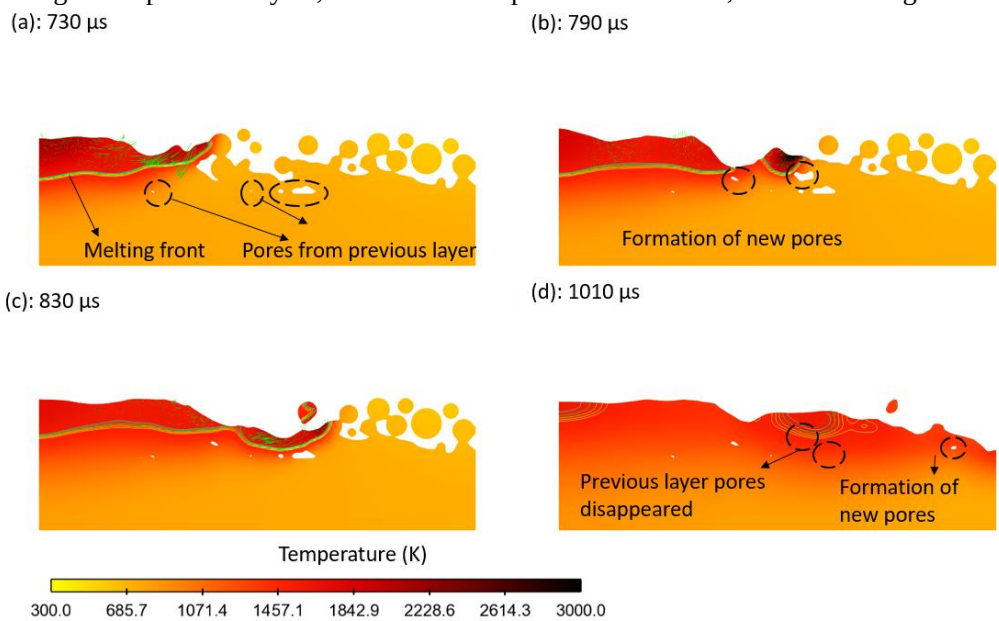

Fig. 9. Fluid region, temperature contour and melt pool dynamics during the scanning of the second layer at y=200 μm (longitudinal cross-section) at: (a) 730 μs, (b) 790 μs, (c) 830 μs and (d) 1010 μs.

Fig. 9 also shows the temperature contour, melt and fluid region in the x-z longitudinal cross-section at y=200 μm. Although the particles are molten by the laser scanning, the

keyhole is not formed at this position since the cross-section is almost 50 µm away from the hotspots formed closer to the center of the beam. At t = 730 µs, there are still a number of remnant pores from the previous layer where the entrapped air could not escape the fluid surface – a phenomena which is again observed at t = 790 µs since the melt region could not penetrate deep enough to capture the void between particles. At t = 830 µs, the pore which had been shaped at t =790 µs is observed to escape the fluid surface. By t = 1010 µs, when the laser has finished scanning the second track, some of the pores trapped from the first layer have escaped the melt region.

To demonstrate the entire scanned block's porosity profile, the fluid region along with its temperature contour are depicted on a number of cross-sections in Fig. 10 at the end of the process for all three layers. As shown in Fig. 10, the pores mostly have irregular shapes, with round edges and sizes spanning between 5 µm to 40 µm. Moreover, the first layer has more lack of fusion zones compared to the second and third layers.

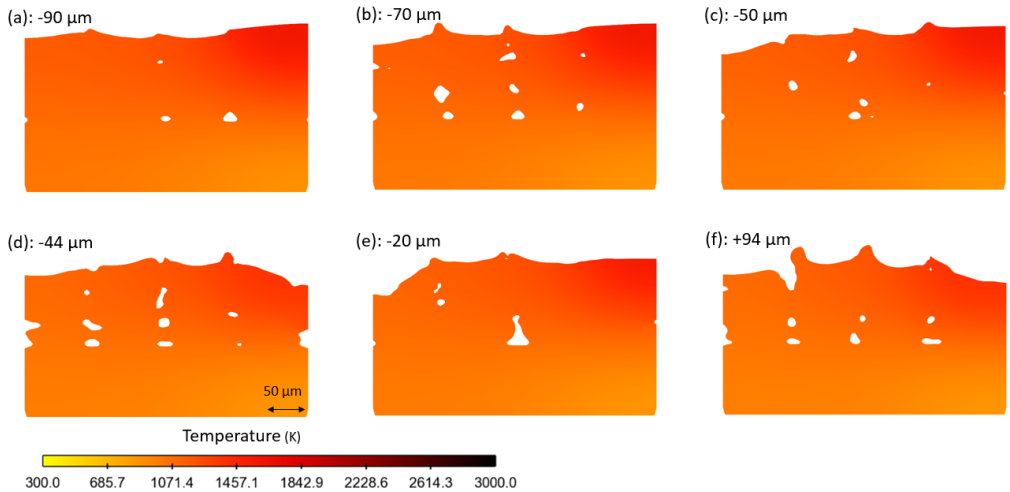

Fig. 10. Fluid region, temperature contour and melt pool dynamics for the whole three layers, at the end of the fusion process for different cross-sections at x: (a) -90 µm, (b) -70 µm, (c) -50 µm, (d) -44 µm, (e) -20 µm and (f) +94 µm.

Furthermore, as observed in Fig. 10 (b), (e) and (f), the pores are mostly created in the area between the melting tracks and stack above each other in a pattern, especially on the lower levels. This stacking pattern of pores is a well-known outcome observed in samples made without rotation or shifting of scanning strategies between successive layers. Based on the image analysis performed on different cross-sections, the porosity due to the lack of fusion is found to be in the range of 0.43 % to 2.54 %.

MECHANICAL ANALYSIS: UNIT CELL

The mechanical response of the unit cell for the upper and lower bounds of porosities are depicted in Fig. 11 and indicates that the porosities have a big influence on the mechanical

behaviour of the samples. As seen in **Fig. 11**, the increase in porosity can reduce the stiffness of the material from a value of 456.7 GPa to 403.2 GPa. The yield limit of the part is affected by the imposed porosities as well, declining from 913 MPa for the unit cell with 0.43 % porosity to 725.8 MPa at 2.54 % porosity. Consequently, these results show that both stiffness and yield limits of the additive manufactured parts can be highly deteriorated because of the presence of even a small amount of porosity.

Fig. 11. Calculated average stress-strain curves for the unit cell for different porosities.

CONCLUSION

In this work, a multi-physics numerical model for the L-PBF process is developed which accounts for multi-phase flow, fluid flow in porous medium, capillary and thermo-capillary forces, solidification and melting, particle-particle interaction, geometry-dependant absorptivity (via ray-tracing method), radiation, , recoil pressure, evaporation and evaporative cooling. The model also implements surface tracking algorithms to capture the evolution of the voids and porosities, which are mainly caused by the lack of fusion zones. The results show that a steep pressure gradient prevails on the melt pool front which pumps the fluid back into the molten regions. Furthermore, the results suggest that the lack of fusion defects are mostly found in the lower layers, where the thermal energy of the fluid is lower, compared to higher levels. A detailed discussion about the formation of the pores is also given, which

reveals that the pores might form, shrink, coalesce and disappear during the course of the process. Moreover, it is found that most of the pores are formed in the lower levels, where more lack of fusion defects are present. The paper also presents a unit cell model developed to capture the effect of the porosities on the mechanical properties, where it is found that an increase in porosity, decreases both the elastic modulus and the yield strength of the material at the same time. Through the combination of the thermo-fluid model and the mechanical unit cell model, a direct link between process parameters of L-PBF and the emergent mechanical properties of the component has been established. Further developments of the meso-scale thermo-fluid model by inclusion of the plasma plume formation, and by tracking the movements of particles and metal droplets dragged by the vapour/gas flow, would lead to better prediction of the surface of the part being manufactured by L-PBF as well as allow a more accurate capturing of the keyhole voids formation/evolution. The usage of representative volume elements to model the mechanical response of the L-PBF parts with porosity will also potentially lead to better results. Further, adding a metallurgical model able to predict phase fractions of the metallic alloy, would provide greater inputs to the mechanical analysis and complete the chain of process-materials-property.

APPENDICES AND ACKNOWLEDGEMENTS

This work has received funding from the European Union Horizon 2020 Marie Skłodowska_Curie ITN PAM^2 project under grant agreement number 721383.

REFERENCES

[1] J.O. MILEWSKI,., 2017. 'Additive Manufacturing of Metals: From Fundamental Technology to Rocket Nozzles, Medical Implants, and Custom Jewelry', *Springer*, Vol. 258., 2017.

[2] T. DEBROY et al., 'Additive manufacturing of metallic components – Process, structure and properties' *Prog. Mater. Sci*., vol. 92, pp. 112–224, 2018.

[3] V. BHAVAR, P. KATTIRE, V. PATIL, S. KHOT, K. GUJAR, and R. SINGH, 'A review on powder bed fusion technology of metal additive manufacturing', *4th International Conference and Exhibition on Additive Manufacturing Technologies-AM-2014*, 2014.

[4] C. KAMATH, B. EL-DASHER, G. F. GALLEGOS, W. E. KING, and A. SISTO, 'Density of additively-manufactured, 316L SS parts using laser powder-bed fusion at powers up to 400 W' *Int. J. Adv. Manuf. Technol.*, vol. 74, no. 1–4, pp. 65–78, 2014.

[5] N. HOPKINSON, R. HAGUE, and P. DICKENS, 'Rapid manufacturing: an industrial revolution for the digital age', *John Wiley & Sons*, 2006.

[6] M. J. MATTHEWS, G. GUSS, S. A. KHAIRALLAH, A. M. RUBENCHIK, P. J. DEPOND, and W. E. KING, 'Denudation of metal powder layers in laser powder bed fusion processes' *Acta Mater.*, vol. 114, pp. 33–42, 2016.

[7] W. E. KING et al., 'Observation of keyhole-mode laser melting in laser powder-bed fusion additive manufacturing' *J. Mater. Process. Technol.*, vol. 214, no. 12, pp. 2915–2925, 2014.

[8] H. GONG, K. RAFI, H. GU, T. STARR, and B. STUCKER, 'Analysis of defect generation in Ti-6Al-4V parts made using powder bed fusion additive manufacturing processes' *Addit. Manuf.*, vol. 1, pp. 87–98, 2014.

[9] N. T. ABOULKHAIR, N. M. EVERITT, I. ASHCROFT, and C. TUCK, 'Reducing porosity in AlSi10Mg parts processed by selective laser melting' *Addit. Manuf.*, vol. 1, pp. 77–86, 2014.

[10] R. LIN, H. PING WANG, F. LU, J. SOLOMON, and B. E. CARLSON, 'Numerical study of keyhole dynamics and keyhole-induced porosity formation in remote laser welding of Al alloys' *Int. J. Heat Mass Transf.*, vol. 108, pp. 244–256, 2017.

[11] P. A. HOOPER, 'Melt pool temperature and cooling rates in laser powder bed fusion' *Addit. Manuf.*, vol. 22, pp. 548–559, 2018.

[12] C. ZHAO et al., 'Real-time monitoring of laser powder bed fusion process using high-speed X-ray imaging and diffraction' *Sci. Rep.*, vol. 7, no. 1, pp. 1–11, 2017.

[13] L. J. ZHANG, J. X. ZHANG, A. GUMENYUK, M. RETHMEIER, and S. J. NA, 'Numerical simulation of full penetration laser welding of thick steel plate with high power high brightness laser' *J. Mater. Process. Technol.*, vol. 214, no. 8, pp. 1710–1720, 2014.

[14] C. BRUNA-ROSSO, A. G. DEMIR, and B. PREVITALI, 'Selective Laser Melting Finite Element Modeling: Validation with High-Speed Imaging and Lack of Fusion Defects Prediction' *Mater. Des.*, vol. 156, pp. 143–153, 2018.

[15] S. MOHANTY AND J. H. HATTEL, 'Numerical model based reliability estimation of selective laser melting process' *Phys. Procedia*, vol. 56, pp. 379–389, 2014.

[16] S. MOHANTY, C. C. TUTUM, AND J. H. HATTEL, 'grid-based scanning path & parametric approach to thermal homogeneity Cellular scanning strategy for selective laser melting : Evolution of optimal grid-based scanning path & parametric approach to thermal homogeneity', *Proceedings of SPIE*, October 2016, 2013.

[17] S. A. KHAIRALLAH, A. T. ANDERSON, A. RUBENCHIK, AND W. E. KING, 'Laser powder-bed fusion additive manufacturing: Physics of complex melt flow and formation mechanisms of pores, spatter, and denudation zones' *Acta Mater.*, vol. 108, pp. 36–45, 2016.

[18] C. QIU, C. PANWISAWAS, M. WARD, H. C. BASOALTO, J. W. BROOKS, and M. M. ATTALLAH, 'On the role of melt flow into the surface structure and porosity development during selective laser melting' *Acta Mater.*, vol. 96, pp. 72–79, 2015.

[19] Y. C. WU et al., 'Numerical modeling of melt-pool behavior in selective laser melting with random powder distribution and experimental validation' *J. Mater. Process. Technol.*, vol. 254, July 2017, pp. 72–78, 2018.

[20] Y. S. LEE AND W. ZHANG, 'Modeling of heat transfer, fluid flow and solidification microstructure of nickel-base superalloy fabricated by laser powder bed fusion' *Addit. Manuf.*, vol. 12, pp. 178–188, 2016.

[21] Z. GAN, H. LIU, S. LI, X. HE, and G. YU, 'Modeling of thermal behavior and mass transport in multi-layer laser additive manufacturing of Ni-based alloy on cast iron' *Int. J. Heat Mass Transf.*, vol. 111, pp. 709–722, 2017.

[22] L. PARRY, I. A. ASHCROFT, and R. D. WILDMAN, 'Understanding the effect of laser scan strategy on residual stress in selective laser melting through thermo-mechanical simulation' *Addit. Manuf.*, vol. 12, pp. 1–15, 2016.

[23] T. ANDRIOLLO and J. H. HATTEL, 'A micro-mechanical analysis of thermo-elastic properties and local residual stresses in ductile iron based on a new anisotropic model for the graphite nodules', *Modelling Simul. Mater. Sci. Eng.*, 24, 2016.

[24] M. TANE, H. NAKAJIMA, Z. REN, and M. VESENJAK, 'Compressive properties of lotus-type porous iron', *Computational Materials Science*, vol. 65, pp. 37–43, 2012.

[25] W. TAN AND Y. C. SHIN, 'Multi-scale modeling of solidification and microstructure development in laser keyhole welding process for austenitic stainless steel' *Comput. Mater. Sci.*, vol. 98, pp. 446–458, 2015.
[26] A. SALEEM, S. FAROOQ, I. A. KARIMI, and R. BANERJEE, 'A CFD simulation study of boiling mechanism and BOG generation in a full-scale LNG storage tank' *Comput. Chem. Eng.*, vol. 115, pp. 112–120, 2018.
[27] S. TIARI, S. QIU, and M. MAHDAVI, 'Discharging process of a finned heat pipe-assisted thermal energy storage system with high temperature phase change materia' *Energy Convers. Manag.*, vol. 118, pp. 426–437, 2016.
[28] V. R. VOLLER and C. PRAKASH, 'A fixed grid numerical modelling methodology for convection-diffusion mushy region phase-change problems' *Int. J. Heat Mass Transf.*, vol. 30, no. 8, pp. 1709–1719, 1987.
[29] H. HAMDI, M. EL GANAOUI, and B. PATEYRON, 'Thermal Effects on the Spreading and Solidification of a Micrometric Molten Particle Impacting onto a Rigid Substrate Thermal Effects on the Spreading and Solidification of a Micrometric Molten Particle Impacting onto a Rigid Substrate' *Fluid Dynamics & Materials Processing*, vol. 8, no. 2, pp. 173–195. (2012).
[30] J. H. CHO and S. J. NA: 'Implementation of real-time multiple reflection and Fresnel absorption of laser beam in keyhole' *J. Phys. D. Appl. Phys*., vol. 39, no. 24, pp. 5372–5378, 2006.
[31] W. TAN, N. S. BAILEY, and Y. C. SHIN: 'Investigation of keyhole plume and molten pool based on a three-dimensional dynamic model with sharp interface formulation' *J. Phys. D. Appl. Phys.*, vol. 46, no. 5, 2013.